entropy

MDPI

Article

Design of Light-Weight High-Entropy Alloys

Rui Feng [1], Michael C. Gao [2,3,*], Chanho Lee [1], Michael Mathes [1], Tingting Zuo [1,4], Shuying Chen [1], Jeffrey A. Hawk [2], Yong Zhang [4] and Peter K. Liaw [1,*]

1 Department of Materials Science and Engineering, The University of Tennessee, Knoxville, TN 37996, USA; rfeng3@vols.utk.edu (R.F.); clee70@vols.utk.edu (C.L.); kmathes1@vols.utk.edu (M.M.); zuott1986.520@163.com (T.Z.); schen38@vols.utk.edu (S.C.)

2 National Energy Technology Laboratory, Albany, OR 97321, USA; jeffrey.hawk@netl.doe.gov

3 AECOM, P.O. Box 1959, Albany, OR 97321, USA

4 State Key Laboratory for Advanced Metals and Materials, University of Science and Technology Beijing, Beijing 100083, China; rzhangy@ustb.edu.cn

* Correspondence: michael.gao@netl.doe.gov (M.C.G.); pliaw@utk.edu (P.K.L.); Tel.: +1-541-967-5869 (M.C.G.); +1-865-974-6356 (P.K.L.)

Academic Editor: An-Chou Yeh

Received: 2 July 2016; Accepted: 5 September 2016; Published: 13 September 2016

Abstract: High-entropy alloys (HEAs) are a new class of solid-solution alloys that have attracted worldwide attention for their outstanding properties. Owing to the demand from transportation and defense industries, light-weight HEAs have also garnered widespread interest from scientists for use as potential structural materials. Great efforts have been made to study the phase-formation rules of HEAs to accelerate and refine the discovery process. In this paper, many proposed solid-solution phase-formation rules are assessed, based on a series of known and newly-designed light-weight HEAs. The results indicate that these empirical rules work for most compositions but also fail for several alloys. Light-weight HEAs often involve the additions of Al and/or Ti in great amounts, resulting in large negative enthalpies for forming solid-solution phases and/or intermetallic compounds. Accordingly, these empirical rules need to be modified with the new experimental data. In contrast, CALPHAD (acronym of the calculation of phase diagrams) method is demonstrated to be an effective approach to predict the phase formation in HEAs as a function of composition and temperature. Future perspectives on the design of light-weight HEAs are discussed in light of CALPHAD modeling and physical metallurgy principles.

Keywords: single-phase solid solutions; intermetallics; phase-formation rules; light-weight HEAs; enthalpy of mixing; entropy of mixing; CALPHAD; excess entropy

1. Introduction

Recently, high-entropy alloys (HEAs) have gained much attention for their ability to expand the limited range of traditional alloys systems and because of their outstanding mechanical properties [1–6]. Due to the demand from transportation and defense industries, the development of a new generation of light-weight alloys has also brought widespread interest in HEAs to the materials science and engineering communities, expressly, for the purpose of saving energy and raw materials [7–15]. The trial-and-error approach that has been used for traditional alloys design is costly and time-consuming for the discovery of new HEAs because of the vast compositional space that they occupy. As a consequence, efforts have been made to study HEA phase-formation rules to accelerate the discovery process [4,16–29]. Taking advantage of the phase-formation rules, the constitutive phases in HEAs can be controlled and adjusted to improve mechanical properties. In recently-developed light-weight HEAs (the densities of light-weight HEAs are defined as less than 7.00 g·cm^{-3} in this paper, considering that most HEAs studied in the literature have densities more

than 7.00 g·cm^{-3}), most of them are composed of solid solutions (SS) and intermetallics (IM), with only a few compositions forming single-phase solid solutions [7,9,11,13,15]. A majority of the light-weight HEAs contain Al and/or Ti in high concentrations in order to lower the density. However, Al (and Ti) tends to form very stable intermetallic compounds with (late) transition-metal elements (TMs) due to the apparent differences in atomic radii and electronegativity. Although Li- and Mg-containing HEAs are reported [30–32], their microstructures show a mixture of various intermetallic compounds.

In order to explore advanced light-weight HEAs, it is essential to adjust the alloy composition, and, thus, the resulting constitutive phases in the microstructure in order to achieve the desired physical and mechanical properties, while keeping the density as low as possible. Therefore, it is important to investigate these empirical phase-formation rules, as applied to light-weight HEAs. Meanwhile, CALPHAD (the acronym of the calculation of phase diagrams) method is also used here to compare the effectiveness of predicting the single-phase solid solutions versus the empirical parameters.

In this regard, many developed formation rules have been summarized and discussed in this paper. The corresponding parameters are also calculated, using these rules, by applying them to a series of developed HEAs and our newly-designed light-weight HEAs, aiming to provide more available experimental data for the assessment of the phase-formation rules in this study. Moreover, the CALPHAD modeling is performed for several equimolar light-weight HEAs. Combined with the experimental results, the phase-prediction effectiveness of the phase-formation rules and CALPHAD method for light-weight HEAs are studied as a way to accelerate the design of new light-weight HEAs with targeted properties.

2. Materials and Methods

Our newly-designed light-weight HEAs comprise of five elements: Al, Cr, Fe, Mn and Ti. To examine the compositional effect on density and phase formation, the Al molar ratio is allowed to vary from 1 to 4. To minimize the formation of detrimental intermetallic compounds, the Ti molar ratio is kept at 1 or 0.25. Strictly speaking, $Al_2CrFeMnTi_{0.25}$, $Al_3CrFeMnTi_{0.25}$, and $Al_4CrFeMnTi_{0.25}$ alloys do not meet the HEA definition (HEAs consist of 5 or more elements between 5 and 35 atomic percent (at.%).) proposed by Yeh et al. [2]. They were designed to explore the lower-density compositional space. In consideration of the possible high-temperature applications, these newly-developed alloys contain Al and Cr in large amounts. The addition of Al (or Cr) holds the potential to form a protective dense surface scale of Al_2O_3 (or Cr_2O_3).

The $Al_xCrFeMnTi_y$ alloys (where the x and y values are in molar ratios: x = 1, 1.5, 2, 3, and 4; and y = 0.25 and 1, respectively) were prepared by arc-melting the constituent elements (element purity > 99.9 weight percentage). To achieve a homogeneous distribution of elements in the alloy, the melting and solidification processes were repeated five times.

The chemical composition and estimated density, ρ, of the alloys are listed in Table 1. Note that the densities of these alloys were estimated, using a rule of mixtures assumption, based on a disordered solid solution, as given by:

$$\rho = \frac{\sum c_i A_i}{\sum \frac{c_i A_i}{\rho_i}} \quad (1)$$

where c_i, A_i, and ρ_i are the atomic percentage, atomic weight, and density of the ith constituent element.

The alloys studied here are in the as-cast state. The crystal structures were identified on the well-polished bulk samples by X-ray diffraction (XRD, Bruker, Billerica, MA, USA), using a Bruker diffractometer with Cu Kα radiation. The microstructures were characterized, by scanning-electron microscopy (SEM, Carl Zeiss, Oberkochen, Germany), using a LEO Gemini 1525 field-emission scanning-electron microscope equipped with the backscattering-electron (BSE, K. E. Developments Ltd., Cambridge, UK) detector and the energy-dispersive X-ray spectrometry (EDX, Oxford Instruments, Abingdon, UK).

Table 1. Nominal chemical composition in at.% and the estimated density, ρ, of the newly-designed $Al_xCrFeMnTi_y$ (x = 1, 1.5, 2, 3, and 4; y = 0.25 and 1) alloys.

Alloy	Al	Cr	Fe	Mn	Ti	ρ (g·cm^{-3})
$Al_{1.5}CrFeMnTi$	27.28	18.18	18.18	18.18	18.18	5.31
$Al_2CrFeMnTi$	33.32	16.67	16.67	16.67	16.67	5.06
$AlCrFeMnTi_{0.25}$	23.53	23.53	23.53	23.53	5.88	5.87
$Al_2CrFeMnTi_{0.25}$	38.10	19.05	19.05	19.05	4.75	5.16
$Al_3CrFeMnTi_{0.25}$	48.00	16.00	16.00	16.00	4.00	4.71
$Al_4CrFeMnTi_{0.25}$	55.17	13.79	13.79	13.79	3.46	4.40

3. Phase-Formation Rules of HEAs

In order to predict the formation of solid solutions in HEAs, many phenomenological parameters based on thermodynamics and physics have been proposed [3,4,6,16,17,19,33]. In this study, several classic models were selected, and their main features are summarized as follows:

Based on thermodynamics and Hume-Rothery rules, Zhang et al. [3,4,16] put forward three parameters to suggest a criterion for the formation of a solid solution: the atomic-radius difference (δ_r), enthalpy of mixing (ΔH_{mix}), and entropy of mixing (ΔS_{mix}). They are defined by Equations (2)–(4), respectively:

$$\delta_r = \sqrt{\sum_{i=1}^{n} c_i(1 - r_i/\overline{r})^2} \tag{2}$$

where $\overline{r} = \sum_{i=1}^{n} c_i r_i$, c_i and r_i are the atomic percentage and radius of the ith element, respectively; and

$$\Delta H_{\mathrm{mix}} = \sum_{i=1, i\neq j}^{n} \Omega_{ij} c_i c_j \tag{3}$$

where $\Omega_{ij} = 4\Delta H_{ij}^{\mathrm{mix}}$, $\Delta H_{ij}^{\mathrm{mix}}$ is the enthalpy of mixing between the ith and jth elements at the equi-molar composition in the liquid using the Miedema model; and

$$\Delta S_{\mathrm{mix}} = -R\sum_{i=1}^{n} (c_i \ln c_i) \tag{4}$$

where R is the gas constant. Note that the configurational entropy of an alloy usually decreases, as the temperature decreases since lowering the temperature promotes developing atomic ordering or separation for the alloy. As a result, the true S_{conf} is temperature dependent, and its temperature dependence can be calculated from hybrid Monte Carlo/molecular dynamics (MC/MD) simulations [34]. Other entropy contributions to solid solutions or intermetallics phases may include the phonon vibration, magnetism, and electron excitation, which can be calculated from first-principles density functional theory (DFT) modeling [35,36].

To further present the balance between the entropy of mixing and the enthalpy of mixing, another parameter, Ω, was also proposed [16,29], as expressed below:

$$\Omega = \frac{T_{\mathrm{m}} \Delta S_{\mathrm{mix}}}{|\Delta H_{\mathrm{mix}}|} \tag{5}$$

where $T_{\mathrm{m}} = \sum_{i=1}^{n} c_i (T_{\mathrm{m}})_i$, $(T_{\mathrm{m}})_i$ stands for the melting point of the ith element.

Based on the existing data for HEAs, the empirical criteria for forming disordered solid solutions in as-cast HEAs were suggested to be $-15 < \Delta H_{\mathrm{mix}} < 5\mathrm{kJ \cdot mol^{-1}}$ and $0\% < \delta_r < 5\%$, or $\Omega \geq 1.1$ and $\delta_r < 6.6\%$.

Recently, for the design of single-phase HEAs, Ye et al. [19] proposed a single thermodynamic parameter, ϕ, taking into account the enthalpy of mixing and the excess entropy of mixing, which results from the dense atomic packing and atomic-size misfit. The single-parameter, ϕ, can be expressed as:

$$\phi = \frac{S_C - S_H}{|S_E|} \tag{6}$$

where $S_C = \Delta S_{\text{mix}}$, and $S_H = \frac{|\Delta H_{\text{mix}}|}{T_{\text{m}}}$. S_E denotes the excess entropy of mixing, which is a function of the atomic packing and atomic size. As reported, a HEA tends to form a single-phase solid solution when $\phi \geq \phi_c$ (ϕ_c is the critical value of ϕ that separates the single-phase solid solution from the multi-phase structures). Otherwise, a multi-phase structure develops when $\phi \leq \phi_c$. Moreover, the ϕ_c is identified to be around 20 according to the investigation of Ye et al. [19].

In fact, the formation of the solid-solution phase or intermetallic phase depends on the competition of the Gibbs free energies between solid solutions and intermetallics. In this regard, King et al. [20] proposed a new parameter, Φ, to describe the competition of the Gibbs free energies between these two phases:

$$\Phi = \left| \frac{\Delta H_{\text{mix}}^{ss} - T_{\text{m}} \Delta S_{\text{mix}}}{\Delta H_f^{Mid}} \right| \tag{7}$$

where $\Delta H_{\text{mix}}^{ss} - T\Delta S_{\text{mix}}$ is the change in the Gibbs free energy for the formation of a fully-disordered solid solution, resulting from a mixture of its individual elements. ΔH_f^{Mid} is the enthalpy of formation of a most stable "hypothetical" intermetallic compound among all the constituent binaries from the constituents of the mixture, while ignoring their entropy since the configurational entropy of intermetallic compounds is usually low or zero [20] and other entropy sources may cancel out between compounds and solid-solution phases [20].

The details to calculate the $\Delta H_{\text{mix}}^{ss}$ and ΔH_f^{Mid} values using the Miedema's model are described in Reference [20], following the approach published in Reference [37]. It should be noted that in general, the calculated $\Delta H_{\text{mix}}^{ss}$ and ΔH_f^{Mid} values, using the Miedema model, have relatively large errors. Therefore, King et al. claimed that when Φ is larger than 1, solid-solution phase will form at the system's melting temperature. The Φ parameters for all the compositions listed in Table 2 were calculated according to Equation (7) via the single phase high-entropy alloys (SPHEAs) program [38].

Another similar criterion based on enthalpy considerations was proposed by Troparevsky et al. [18]. They used the enthalpy of formation of binary compounds that are predicted, using DFT calculations in the literature. Based on the calculated enthalpy matrix, it was claimed that a single-phase solid solution would form if the enthalpies of formation of all possible binary compounds fall within a specified range. This range requires binary compounds to be neither too stable, leading to the precipitation of that compound, nor unstable, indicating the immiscibility of the constituent elements. Using the enthalpy of the formation matrix provided in Reference [18], a parameter, Φ_f (similar to Φ), is calculated, which is expressed as follows.

$$\Phi_f = \frac{T_{\text{ann}} \Delta S_{\text{mix}}}{\left| \Delta H_f^{\text{DFT}} \right|} \tag{8}$$

here, T_{ann} is the annealing temperature used to achieve the corresponding equilibrium state in the experiments, and an appropriate value is suggested to be $T_{\text{ann}} = 0.55 T_{\text{m}}$ in the work of Troparevsky et al. [18]. Values in the enthalpy of formation matrix in Reference [18] were used for ΔH_f to calculate Φ_f. This model ignores the enthalpy of solid-solution phases and the entropy of intermetallic compounds.

Utilizing these developed phase-formation rules mentioned above, the entirety of the corresponding empirical parameters was calculated, based on existing and newly-designed light-weight HEAs (density < 7.00 g·cm^{-3}). In addition, several classic HEAs are selected to compare with the light-weight HEAs. These parameters are listed in Table 2. For a comprehensive list of single-phase HEAs in face-centered cubic (FCC) [1,3,6], body-centered cubic (BCC) [3,6,39], or hexagonal close-packed (HCP) [3,6,7,40–42] structures that are experimentally verified or computationally predicted, the reader is referred to a recent publication [26]. It should be noted that the listed alloys in Table 2 were in the as-cast state, except for $Al_{20}Li_{20}Mg_{10}Sc_{20}Ti_{30}$ and AlFeMgTiZn, which were produced by mechanical alloying.

Table 2. The microstructures and the formation-rule parameters, for typical and light-weight HEAs reported and newly-designed HEAs.

Number	Alloys	Density * ($g \cdot cm^{-3}$)	Structure	δ_r(%)	ΔH_{mix}($kJ \cdot mol^{-1}$)	ΔS_{mix}($kJ \cdot mol^{-1}$)	T_m(°C)	Ω	ϕ	Φ	Φ_f	Reference
1	$Al_{1.5}CrFeMnTi$	5.31	BCC + $L2_1$ + Laves	6.41	−17.98	13.25	1336.31	1.19	1.63	0.31	0.28	Current work
2	$Al_2CrFeMnTi$	5.06	BCC + $L2_1$ + Laves	6.33	−19.00	12.98	1279.99	1.06	0.59	0.34	0.27	Current work
3	$AlCrFeMnTi_{0.25}$	5.87	BCC + $L2_1$	5.78	−12.07	12.71	1357.29	1.72	4.61	0.37	0.28	Current work
4	$Al_2CrFeMnTi_{0.25}$	5.16	BCC + $L2_1$	6.07	−14.80	12.14	1224.56	1.23	1.93	0.42	0.24	Current work
5	$Al_3CrFeMnTi_{0.25}$	4.71	BCC + $L2_1$ + Laves	6.02	−16.04	11.53	1142.71	1.02	0.16	0.46	0.25	Current work
6	$Al_4CrFeMnTi_{0.25}$	4.40	BCC + $L2_1$ + Laves	5.86	−15.71	10.73	1077.10	0.92	−0.92	0.48	0.22	Current work
7	$AlCr_{0.5}NbTiV$	5.71	BCC	4.55	−15.41	13.15	1704.22	1.69	6.94	0.31	0.35	[11]
8	AlCrNbTiV	5.82	BCC + Laves	5.19	−14.56	13.38	1724.49	1.84	6.18	0.31	0.36	[11]
9	$AlCr_{1.5}NbTiV$	5.90	BCC + Laves	5.55	−13.75	13.25	1741.09	1.94	5.72	0.30	0.36	[11]
10	AlFeMgTiZn	4.34	BCC + IM	6.04	−6.44	13.38	987.23	2.62	4.44	1.66×10^{-2}	0.18	[30]
11	AlLiMgZnSn	4.23	FCC + IM	5.33	−6.08	13.38	428.58	1.54	4.72	8.39×10^{-3}	0.10	[31]
12	$AlLi_{0.5}MgZn_{0.5}Sn_{0.2}$	3.22	FCC+ IM	5.66	−3.89	12.31	517.83	2.50	7.93	8.73×10^{-3}	0.11	[31]
13	$AlLi_{0.5}MgZn_{0.5}Cu_{0.2}$	3.73	FCC + IM	6.72	−3.30	12.31	571.13	3.15	7.04	1.25×10^{-2}	0.11	[31]
14	$AlLi_{0.5}MgCu_{0.5}Sn_{0.2}$	3.69	FCC + IM	7.60	−3.65	12.31	621.76	3.02	4.99	1.29×10^{-2}	0.12	[31]
15	$Al_{80}Li_5Mg_5Zn_5Sn_5$	3.05	FCC + IM	3.61	−0.53	6.47	602.50	10.68	12.58	4.66×10^{-3}	0.06	[31]
16	$Al_{80}Li_5Mg_5Zn_5Cu_5$	3.08	FCC + IM	4.10	−0.61	6.47	645.13	9.73	12.07	4.92×10^{-3}	0.07	[31]
17	$Al_{20}Li_{20}Mg_{10}Sc_{20}Ti_{30}$	2.67	FCC	5.30	−0.40	12.95	1041.83	42.56	16.17	6.27×10^{-4}	0.22	[7]
18	$AlNb_{1.5}Ta_{0.5}Ti_{1.5}Zr_{0.5}$	6.88	BCC	3.07	−15.12	12.51	1862.79	1.77	14.71	0.27	0.28	[15]
19	AlNbTiV	5.59	BCC	3.30	−16.25	11.53	1678.87	1.38	7.22	0.30	0.30	[9]
20	$Al_{0.5}NbTiVZr$	6.04	BCC + Laves + Zr_2Al	6.67	−10.86	13.15	1831.16	2.55	6.18	0.25	0.29	[10]
21	AlNbTiVZr	5.79	BCC + Laves + Zr_2Al	5.53	−17.44	13.38	1714.09	1.52	3.91	0.23	0.28	[10]
22	$Al_{1.5}NbTiVZr$	5.55	BCC + Laves + Zr_2Al	5.32	−21.55	13.25	1618.31	1.16	1.71	0.25	0.27	[10]
23	CrNbTiZr	6.67	BCC + Laves	7.84	−5.00	11.53	1976.75	5.19	4.31	0.66	0.40	[13]
24	CrNbTiVZr	6.57	BCC + Laves	7.67	−4.64	13.38	1963.40	6.45	5.24	0.79	0.46	[13]
25	NbMoCrTiAl	6.57	BCC + IM	4.87	−13.60	13.38	1867.09	2.11	8.32	0.32	0.38	[14]
26	NbTiVZr	6.52	BCC	6.03	−0.25	11.53	1977.50	103.76	7.97	1.86	2.64	[13]
27	$NbTiV_2Zr$	6.34	3 BCCs	6.41	−1.28	11.08	1964.00	19.36	6.43	1.88	2.52	[13]
28	CoCrFeNi **	8.19	FCC	1.03	−3.75	11.53	1598.75	5.75	3583.31	1.16	1.27	[43]
29	CoCrFeMnNi **	8.04	FCC	0.92	−4.16	13.38	1528.20	5.79	34.68	1.12	1.19	[1]
30	HfNbTiZr **	8.38	BCC	4.12	2.50	11.53	2058.25	10.75	15.26	1.95	6.96	[44]
31	HfNbTaTiZr **	9.94	BCC	4.01	2.72	13.38	2250.00	12.41	16.90	2.55	8.75	[45]
32	MoNbTaW **	13.80	BCC	2.27	−6.50	11.53	2884.75	5.60	60.98	1.71	1.08	[39]
33	MoNbTaVW **	13.63	BCC	3.21	−4.64	13.38	2689.80	8.54	41.17	1.75	1.17	[39]

* If there are no experimental densities provided, the densities will be calculated using Equation (1). ** Listed for comparison purposes.

4. Results

4.1. Newly-Designed Light-Weight HEAs

Figure 1 shows the XRD patterns of our newly-designed light-weight $Al_xCrFeMnTi_y$ HEAs. All major phases are identified. For clarity, unknown phases are not indexed. The XRD results show that all the alloys exhibit the presence of a BCC structure. Besides the fundamental diffraction peaks for the BCC structure, two peaks at about 26° and 30° are detected for all the six compositions, and they are identified as the Fe_2AlTi-type $L2_1$ structure. The XRD patterns also show the existence of the intermetallic C14 Laves phase in $Al_{1.5}CrFeMnTi$ (Figure 1e) and $Al_2CrFeMnTi$ (Figure 1f) alloys. In addition to BCC and $L2_1$ phases, some complex structures are reflected in $Al_3CrFeMnTi_{0.25}$ (Figure 1c) and $Al_4CrFeMnTi_{0.25}$ (Figure 1d), which are identified as Al_8Cr_5-type (cI52, I-43m) and $Al_{58.5}Cr_{10.3}Fe_{31.2}$-type (hR26, R3m) phases.

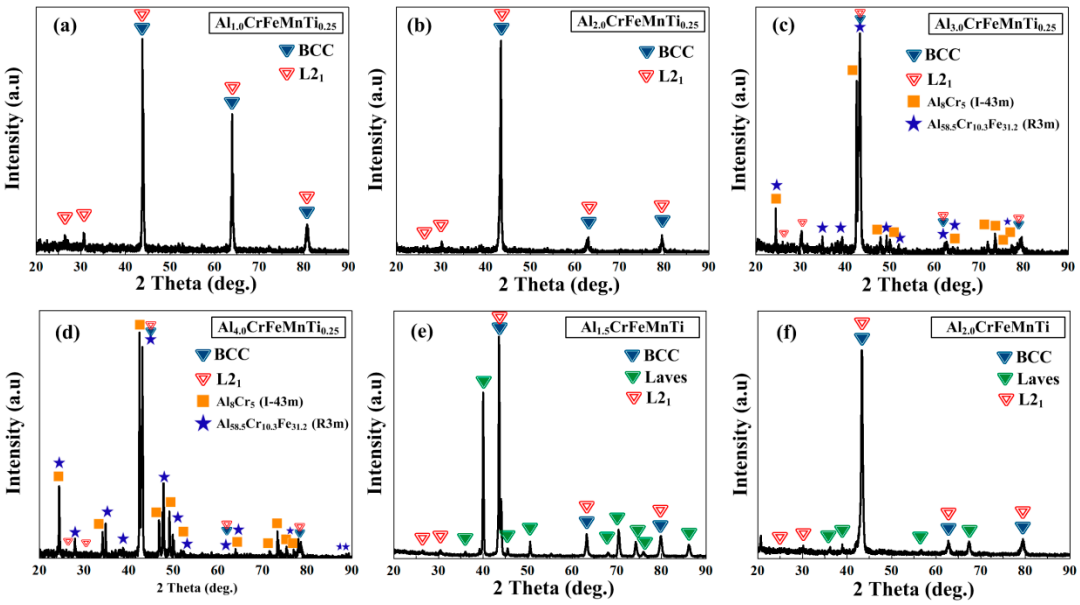

Figure 1. XRD patterns of a series of newly-designed light-weight HEAs: (**a**) $Al_{1.0}CrFeMnTi_{0.25}$; (**b**) $Al_{2.0}CrFeMnTi_{0.25}$; (**c**) $Al_{3.0}CrFeMnTi_{0.25}$; (**d**) $Al_{4.0}CrFeMnTi_{0.25}$; (**e**) $Al_{1.5}CrFeMnTi$ and (**f**) $Al_{2.0}CrFeMnTi$.

The microstructures of these light-weight HEAs were characterized by SEM, as shown in Figure 2. Alloys of $Al_3CrFeMnTi_{0.25}$ (Figure 2c), $Al_{1.5}CrFeMnTi$ (Figure 2e), and $Al_2CrFeMnTi$ (Figure 2f) all exhibit multi-phase structures, while $AlCrFeMnTi_{0.25}$ (Figure 2a) and $Al_2CrFeMnTi_{0.25}$ (Figure 2b) present a main BCC structure. It is worth noting that the SEM micrograph does not show enough phase contrast between phases in the microstructure of $Al_4CrFeMnTi_{0.25}$ (Figure 2d), although multiple phases are detected, using XRD (Figure 1d). The black dots appearing on the SEM images are defects produced during the casting process. Since one main purpose of the experimental part provided here is to provide more available experimental data to assess the phase-formation rules, the evidence showing single-phase or multi-phase structures is sufficient in this study.

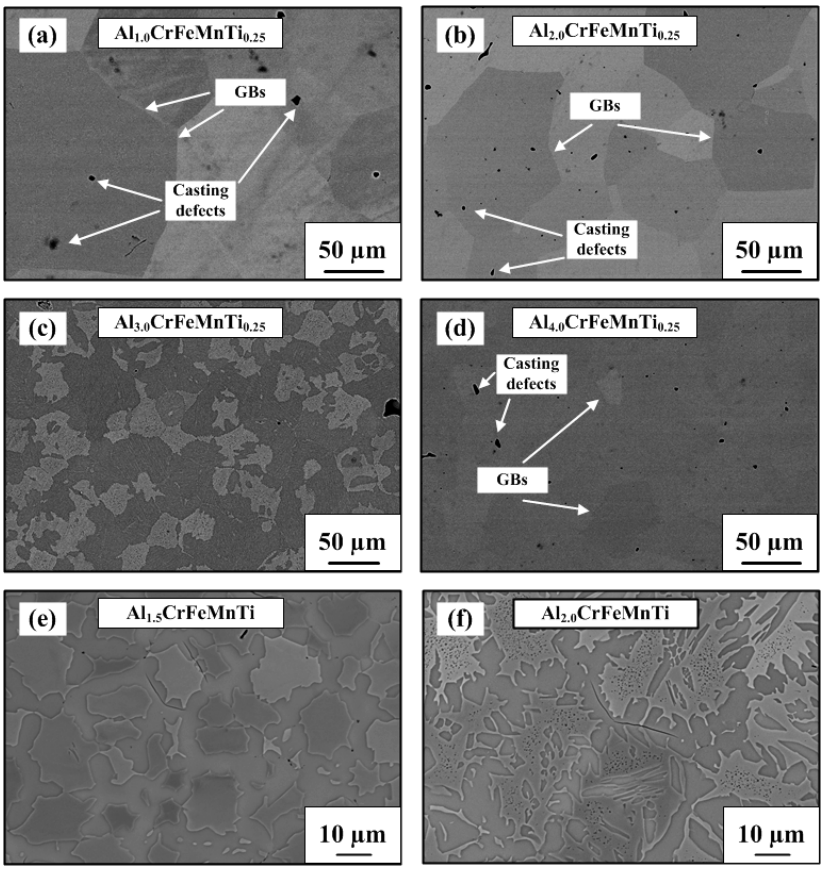

Figure 2. SEM images of a series of newly-designed light-weight HEAs: (**a**) $Al_{1.0}CrFeMnTi_{0.25}$; (**b**) $Al_{2.0}CrFeMnTi_{0.25}$; (**c**) $Al_{3.0}CrFeMnTi_{0.25}$; (**d**) $Al_{4.0}CrFeMnTi_{0.25}$; (**e**) $Al_{1.5}CrFeMnTi$ and (**f**) $Al_{2.0}CrFeMnTi$. (GBs represent grain boundaries).

4.2. Criteria Based on ΔH_{mix}, δ_r, and Ω

As previously reported, in order to form disordered solid solutions in the as-cast HEAs, the enthalpy of mixing and atomic-radius difference rules suggested that $-15 < \Delta H_{\mathrm{mix}} < 5\mathrm{kJ}\cdot\mathrm{mol}^{-1}$ and $0 < \delta_r < 5\%$ [4]. For the Ω parameter, solid solutions will form in the range of $\Omega \geq 1.1$ and $\delta_r < 6.6\%$ [16]. The relationship among the three parameters is plotted in two maps, as shown in Figure 3a,b. In Figure 3, the "SS + IM" symbol refers to the alloys showing multi-phase structure (i.e., solid-solution and intermetallic phases) listed in Table 2. The "SS (Light-weight HEAs)" symbol represents those light-weight HEAs forming single-phase solid solutions. The "SS (Classic HEAs)" symbol stands for those selected classic HEAs (Table 2) with single-phase solid solutions. Moreover, each composition symbol in Figure 3 (and Figures 4–7) is marked with a number, which has the one-to-one correspondence with the composition's number listed in Table 2. The shaded area in yellow color refers to the region where the vast majority of the compositions form a single solid solution, whereas the shaded area in blue color refers to the region where the vast majority of the compositions form "SS + IM." Note all the symbols and the shading color scheme in the following maps in Figures 4–7 have the same meaning. Figure 3a shows the relationship between the enthalpy of mixing (ΔH_{mix}) and atomic-radius difference (δ_r) for a series of previously-developed, classic HEAs and light-weight HEAs. The single-phase classic and light-weight HEAs are located in a range of $-16.25 \leq \Delta H_{\mathrm{mix}} < 5\mathrm{kJ}\cdot\mathrm{mol}^{-1}$ and $0\% < \delta_r < 6.6\%$.

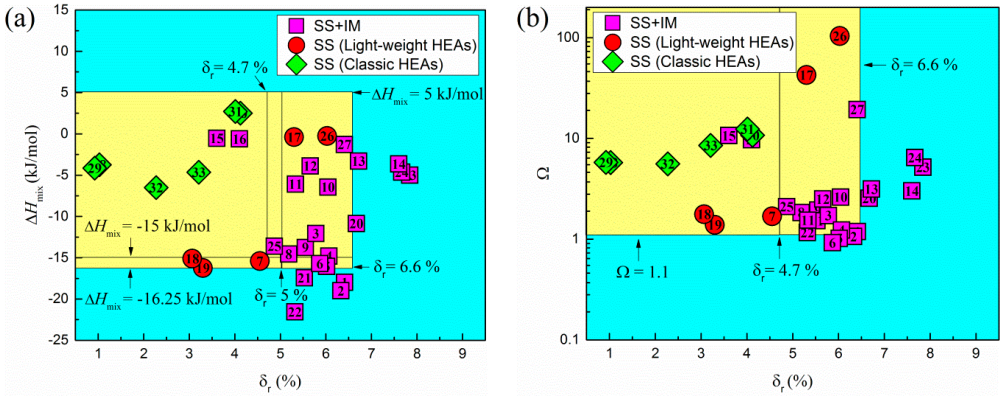

Figure 3. Plots of (**a**) ΔH_{mix} and (**b**) Ω versus δ_r for a series of the developed classic HEAs and light-weight HEAs (each composition symbol shown in Figures 3–7 is marked with the same composition's number shown in Table 2).

The $\Omega - \delta_r$ relation presented in Figure 3b shows that all the single-phase solid-solution HEAs in this study fall into the suggested "yellow" range of $\Omega \geq 1.1$ and $\delta_r < 6.6\%$. However, many multi-phase HEAs are also located in the range of $4.7\% < \delta_r < 6.6\%$. In fact, it can be clearly seen that a stricter criterion ($\Omega \geq 1.1$ and $\delta_r < 4.7\%$) exists, compared with the reported criterion ($\Omega \geq 1.1$ and $\delta_r < 6.6\%$) [16], which separates the single-phase solid solutions from multi-phases structures in HEAs. In addition, two exceptional light-weight HEAs having δ_r larger than 4.7% are $Al_{20}Li_{20}Mg_{10}Sc_{20}Ti_{30}$ and NbTiVZr [7,13]. Note that the $Al_{20}Li_{20}Mg_{10}Sc_{20}Ti_{30}$ alloy [7] was produced by the mechanical-alloying method. Thus, the as-synthesized alloy may be far away from its thermodynamic equilibrium, and large internal strains will inevitably be introduced into the alloys after mechanical-alloying. Therefore, this criterion may not be applicable to this alloy. The NbTiVZr alloy [15] has δ_r = 6.03%, but its Ω = 103.76 is the largest among all the HEAs in this study (Table 2). The results shown in Figure 3 demonstrate that: (1) the δ_r parameter is superior to ΔH_{mix} or Ω; and (2) the critical δ_r value lies in a range of 4.7%–6.6%, depending on alloy compositions.

4.3. Criteria Based on ϕ, Φ, and Φ_f

To integrate the effects of thermodynamics and atomic packing on the phase formation, the single thermodynamic parameter (ϕ) [19] for selected classic HEAs and light-weight HEAs was calculated. Then, plots of ϕ against ΔH_{mix}, δ_r, and Ω are presented in Figure 4 to look into the potential criteria through combing these parameters. It can be clearly seen that there is a clear boundary separating the region of solid solutions (in yellow color) from the region of solid solutions + intermetallics (in blue color) based on the ϕ values. The critical, ϕ_c, which is used to separate the two regions, is about 7, while in Reference [19] this value is about 20. This trend implies that the values of ϕ in light-weight HEAs are somewhat smaller than those classic HEAs. This trend is mainly related to the fact that the light-weight HEAs usually have more negative ΔH_{mix}, which results in the decrease of ϕ (see Equation (6)). Even so, it can be hypothesized that the thermodynamic parameter, ϕ, is still somewhat effective to distinguish the region of solid solutions and that of solid solutions + intermetallics, which is helpful for the design of new light-weight HEAs.

The hypothesis for the parameters, Φ and Φ_f, is that the phase stability of an HEA is decided by the competition in the Gibbs free energies between the solid solution and intermetallic phases at constant temperature and pressure. This hypothesis makes it possible to perform computer screening for single-phase solid solutions in a system of an arbitrary number of components. To examine the effectiveness of both parameters with the same physical meaning but different models in the present study, the relations between Φ and Φ_f with respect to ΔH_{mix}, δ_r, and Ω for all alloys listed in Table 2 are illustrated in Figures 5 and 6, respectively. Through the observation of these newly-produced

plots, it is important to study if the combination of different rules would generate meaningful results, meanwhile, finding flaws in the currently-reported rules.

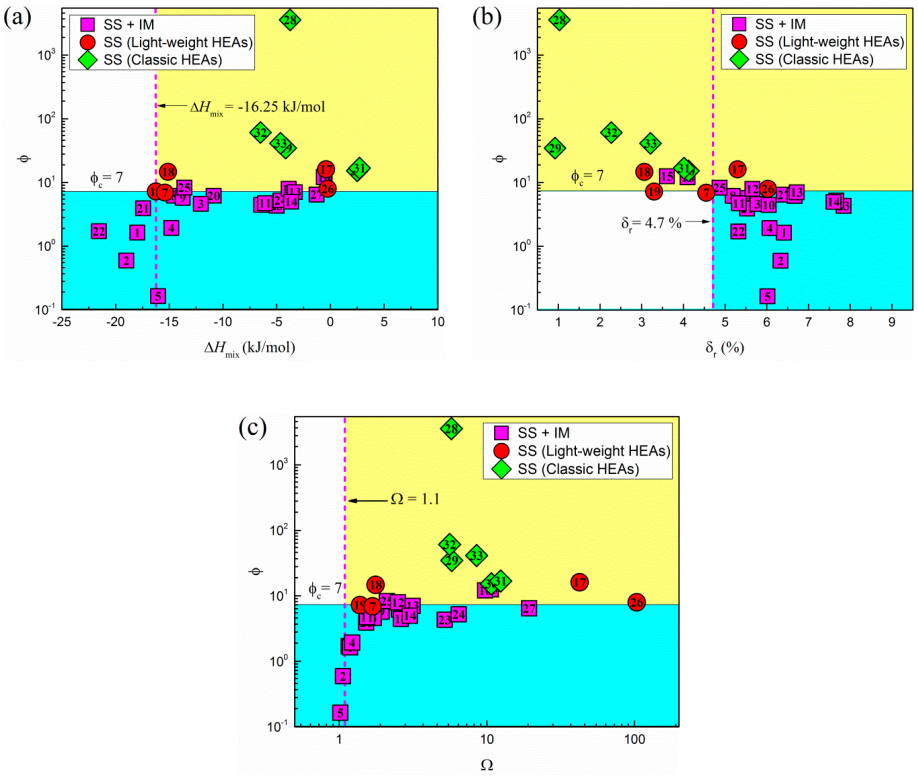

Figure 4. The variation of the single-parameter, ϕ, with respect to (**a**) ΔH_{mix}, (**b**) δ_r, and (**c**) Ω.

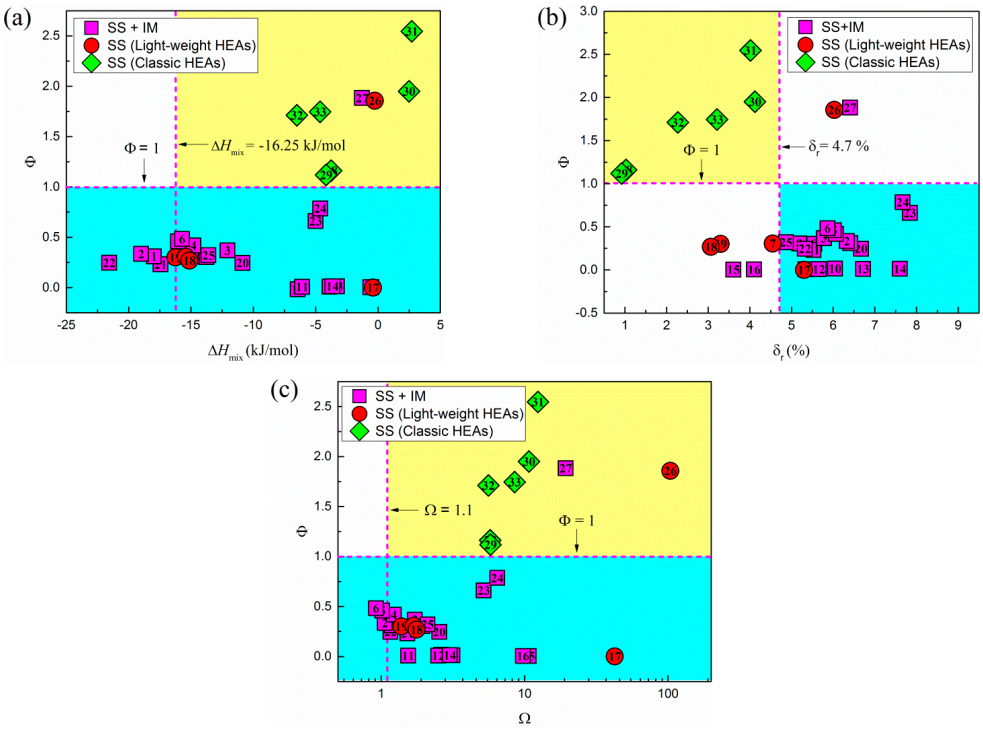

Figure 5. The variation of the thermodynamic parameter, Φ, with respect to (**a**) ΔH_{mix}, (**b**) δ_r, and (**c**) Ω.

In Figures 5 and 6, it can be clearly seen that both Φ and Φ_f criteria ($\geq$1) fail to predict the formation of the light-weight single-phase solid solution (such as AlNbTiV in Table 2), though they can predict the classic single-phase HEAs successfully. Most of the light-weight single-phase HEAs are located in the "blue" region well below the dashed lines, Φ and $\Phi_f = 1$, e.g., the calculated Φ and Φ_f values for single-phase AlNbTiV are 0.30 (Table 2). One exception is the single-phase NbTiVZr [15] alloy, which has Φ and Φ_f values of 1.86 and 2.64 (Table 2), respectively, despite its relatively-large $\delta_r = 6.03\%$. Conversely, although the $NbTiV_2Zr$ alloy also has large Φ and Φ_f values, it does not form the single-phase solid-solution structure, which may result from the larger atomic-radius difference ($\delta_r = 6.41\%$). In short, relying on Φ or Φ_f criterion alone cannot predict the formation of light-weight single-phase solid solutions.

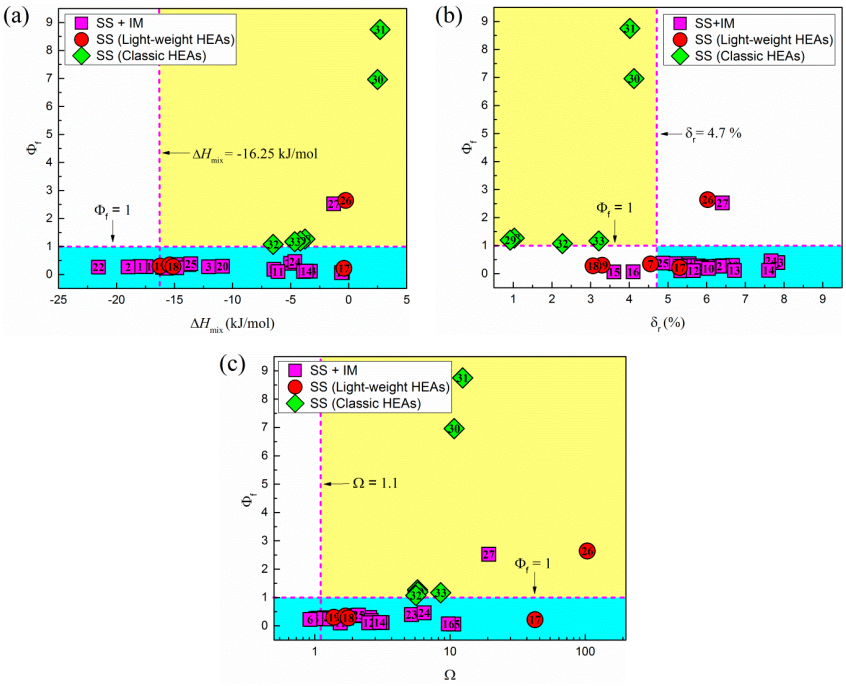

Figure 6. The variation of thermodynamic parameter Φ_f with respect to (**a**) ΔH_{mix}, (**b**) δ_r, and (**c**) Ω.

Although the region of solid solutions and region of solid solutions + intermetallics cannot be distinguished, using Φ or Φ_f values ($\geq$1) alone, the combination of Φ or Φ_f with the atomic-radius difference, δ_r appears to be more effective criteria than with ΔH_{mix}, or Ω, as demonstrated in Figures 5 and 6. In other words, when Φ or Φ_f is less than 1, single-phase solid solutions may still form if the atomic-radius difference is sufficiently small (In this study, δ_r should be less than the 4.7%). On the other hand, even if δ_r is larger than 4.7%, large Φ or Φ_f parameters may still promote forming single-phase solid solution, as in the NbTiVZr alloy (Table 2). In fact, the formation of single-phase solid solutions is the result of the synergy of the thermodynamic factors, atomic-size effects, and other factors. Therefore, thermodynamic factors and atomic-size effects must be considered together when predicting the phase formation of light-weight HEAs.

Furthermore, in order to find more meaningful phase-formation criteria by combing different rules, $\Phi_f$versus ϕ, and $\Phi_f$versus Φ are plotted in Figure 7. In Figure 7a, the yellow area represents the region forming single-phase solid solutions, while the blue region stands for the area forming single-phase solid solutions plus intermetallic phases, and they are separated by the $\phi_c = 7$. In Figure 7b, the selected alloys are divided to four regions by the dash lines $\Phi_f = 1$ and $\Phi = 1$. In examining the two plots, it is obvious that the combinations of the thermodynamic parameters can only correctly predict the formation of single-phase solid solutions in classic HEAs, while failing to predict the formation of single-phase solid solutions in light-weight HEAs.

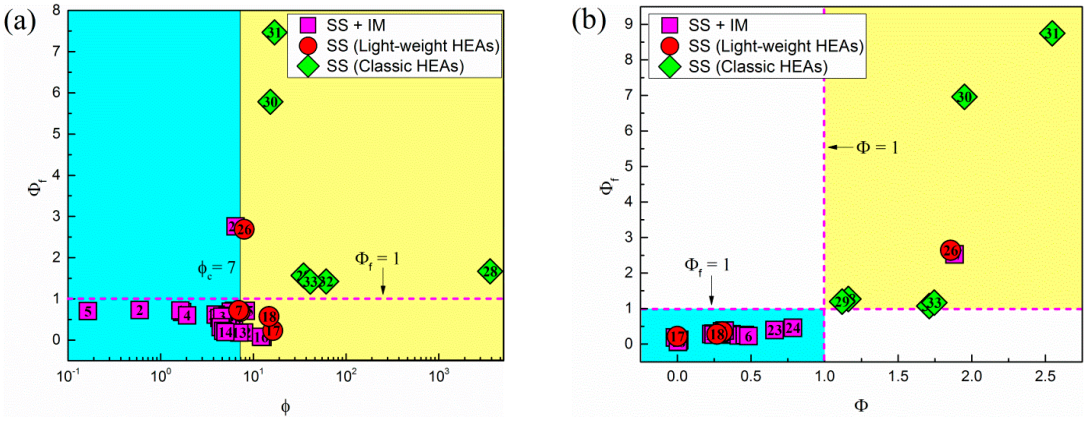

Figure 7. Comparison plots of (**a**) Φ_f versus ϕ and (**b**) Φ_f versus Φ.

4.4. CALPHAD Modeling

As shown in Table 3, empirical rules do not always correctly predict the formation of single-phase solid solutions, and actually none of them works for all the compositions studied. Furthermore, they will not predict the crystal structure of the solid solution or compound phase either. In contrast, the CALPHAD method determines the Gibbs free energies of all phases in the system as a function of composition and temperature, and, thus, is the ideal tool for predicting the phase formation in multi-component systems, such as HEAs, provided that the database is sufficiently reliable.

Table 3. The effectiveness of the phase-formation prediction for light-weight HEAs using the empirical phase-formation rules ($\surd$ and $\times$ represent successful and unsuccessful predictions, respectively).

Alloys	Structure	ΔH_{mix} vs. δ_r	Ω vs. δ_r	ϕ	Φ	Φ_f
$Al_{1.5}CrFeMnTi$	BCC + $L2_1$ + Laves	$\surd$	$\times$	$\surd$	$\surd$	$\surd$
$Al_2CrFeMnTi$	BCC + $L2_1$ + Laves	$\surd$	$\surd$	$\surd$	$\surd$	$\surd$
$AlCrFeMnTi_{0.25}$	BCC + $L2_1$	$\surd$	$\times$	$\surd$	$\surd$	$\surd$
$Al_2CrFeMnTi_{0.25}$	BCC + $L2_1$	$\surd$	$\times$	$\surd$	$\surd$	$\surd$
$Al_3CrFeMnTi_{0.25}$	BCC + $L2_1$ + Laves	$\surd$	$\surd$	$\surd$	$\surd$	$\surd$
$Al_4CrFeMnTi_{0.25}$	BCC + $L2_1$ + Laves	$\surd$	$\surd$	$\surd$	$\surd$	$\surd$
$AlCr_{0.5}NbTiV$	***BCC***	$\times$	$\surd$	$\surd$	$\times$	$\times$
AlCrNbTiV	BCC + Laves	$\surd$	$\times$	$\surd$	$\surd$	$\surd$
$AlCr_{1.5}NbTiV$	BCC + Laves	$\surd$	$\times$	$\surd$	$\surd$	$\surd$
AlFeMgTiZn	BCC + IM	$\surd$	$\times$	$\surd$	$\surd$	$\surd$
AlLiMgZnSn	FCC + IM	$\surd$	$\times$	$\surd$	$\surd$	$\surd$
$AlLi_{0.5}MgZn_{0.5}Sn_{0.2}$	FCC + IM	$\surd$	$\times$	$\times$	$\surd$	$\surd$
$AlLi_{0.5}MgZn_{0.5}Cu_{0.2}$	FCC + IM	$\surd$	$\surd$	$\times$	$\surd$	$\surd$
$AlLi_{0.5}MgCu_{0.5}Sn_{0.2}$	FCC + IM	$\surd$	$\surd$	$\surd$	$\surd$	$\surd$
$Al_{80}Li_5Mg_5Zn_5Sn_5$	FCC + IM	$\times$	$\times$	$\times$	$\surd$	$\surd$
$Al_{80}Li_5Mg_5Zn_5Cu_5$	FCC + IM	$\times$	$\times$	$\times$	$\surd$	$\surd$
$Al_{20}Li_{20}Mg_{10}Sc_{20}Ti_{30}$	***FCC***	$\times$	$\surd$	$\surd$	$\times$	$\times$
$AlNb_{0.5}Ta_{0.5}Ti_{1.5}Zr_{0.5}$	***BCC***	$\times$	$\surd$	$\surd$	$\times$	$\times$
AlNbTiV	***BCC***	$\times$	$\surd$	$\surd$	$\times$	$\times$
$Al_{0.5}NbTiVZr$	BCC + Laves + Zr_2Al	$\surd$	$\surd$	$\surd$	$\surd$	$\surd$
AlNbTiVZr	BCC + Laves + Zr_2Al	$\surd$	$\times$	$\surd$	$\surd$	$\surd$
$Al_{1.5}NbTiVZr$	BCC + Laves + Zr_2Al	$\surd$	$\times$	$\surd$	$\surd$	$\surd$
CrNbTiZr	BCC + Laves	$\surd$	$\surd$	$\surd$	$\surd$	$\surd$
CrNbTiVZr	BCC + Laves	$\surd$	$\surd$	$\surd$	$\surd$	$\surd$
NbMoCrTiAl	BCC + IM	$\times$	$\times$	$\times$	$\surd$	$\surd$
NbTiVZr	***BCC***	$\times$	$\surd$	$\surd$	$\surd$	$\surd$
$NbTiV_2Zr$	3 BCCs	$\surd$	$\times$	$\surd$	$\times$	$\times$

Single-phase solid-solution HEAs are highlighted by Italic and bold types.

The empirical rules evaluated in this study except the Ω and ϕ parameters fail for single-phase AlNbTiV and $AlCr_{0.5}NbTiV$ alloys. For the single BCC NbTiVZr, the Ω, ϕ, Φ, and Φ_f parameters work while the $\Delta H_{\mathrm{mix}} - \delta_r$ rule fails. On the other hand, all empirical rules work well for AlCrNbTiV, CrNbTiZr, and CrNbTiVZr, except that the $\Omega - \delta_r$ rule fails for AlCrNbTiV, and these alloys show a mixture of the BCC solid solution with Laves phases.

To demonstrate the effectiveness in predicting the phase stability for light-weight HEAs, the CALPHAD calculations were carried out on selected compositions using the TCNI8 thermodynamic database supplied by ThermoCalc^{TM} (version 2015b, Thermo-Calc Software, Stockholm, Sweden) [46]. This database covers the complete binaries pertaining to elements, Al, Cr, Nb, Ti, V, and Zr, which are important for light-weight HEAs. The previous CALPHAD modeling using this database demonstrated good agreement with the experimental observations for various refractory BCC HEAs [27,47–51]. The reader is referred to several recent publications [22,50–54] for guidance on the CALPHAD modeling of HEAs. The predicted phase stability during solidification for these alloys is shown in Figure 8.

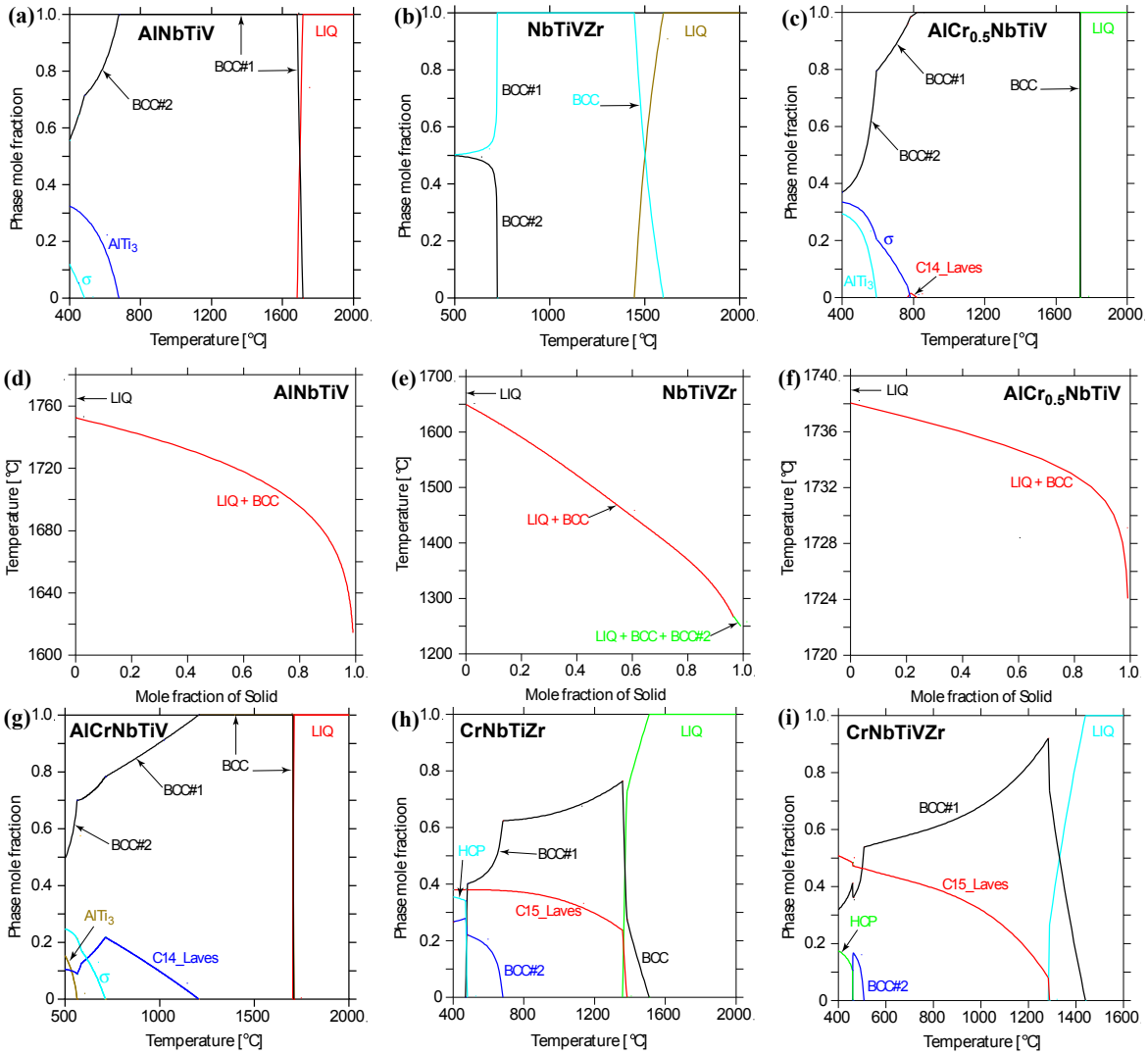

Figure 8. Predicted phase formation in (**a**,**d**) AlNbTiV, (**b**,**e**) NbTiVZr; (**c**,**f**) $AlCr_{0.5}NbTiV$; (**g**) AlCrNbTiV; (**h**) CrNbTiZr and (**i**) CrNbTiVZr using the TCNI8 database. The non-equilibrium solidification for plots (**d**–**f**) are generated using the Scheil model [52].

For AlNbTiV at equilibrium (Figure 8a), the database correctly predicts the formation of the BCC phase over an extremely wide temperature range. The primary BCC phase starts to form at T = 1752 °C; the solidus temperature (T_{sol}) is 1717 °C. At the decomposition temperature (T_{dec}) of 679 °C, the primary BCC phase decomposes to a Ti-poor BCC phase and $AlTi_3$_DO19 phase. The σ phase forms at T ≤ 485 °C. The ratio of the temperature range where the primary BCC phase is stable over the solidus temperature, namely, $(T_{sol} - T_{dec})/T_{sol}$, is 0.52. Gao [26] suggested that a ratio ≥0.3 typically favors the formation of a single-phase solid solution in the as-cast state. Due to slow diffusivities at low temperatures, it is unlikely to observe the BCC decomposition in a normal laboratory condition. The non-equilibrium solidification simulation was accomplished, using the Scheil–Gulliver models [55,56], which assume equilibrium mixing in the liquid and no diffusion in solids. The simulation also predicts the formation of a single BCC solid-solution phase, as shown in Figure 8d.

Similarly, CALPHAD modeling predicts the likely formation of a single BCC phase for NbTiVZr in the as-cast state (Figure 8b,e). The BCC phase forms at T ≤ 1650 °C; the solidus temperature is 1465 °C. At T = 723 °C, the BCC phase decomposes to the BCC#1 phase that is rich in Zr and Ti, and the BCC#2 phase that is rich in V and Nb. The calculated ratio of $(T_{sol} - T_{dec})/T_{sol}$ is 0.43. Although the Scheil simulation predicts the formation of an additional BCC phase towards the end of the non-equilibrium solidification, its mole fraction is less than 1%, and its presence may not be detectable if any was to form in the alloy.

For $AlCr_{0.5}$NbTiV (Figure 8c), the database predicts that the BCC phase forms at T ≤ 1739 °C; the solidus temperature is 1734 °C. The C14 Laves phase forms in a narrow temperature range (765–819 °C). The σ phase forms at T ≤ 782 °C. As the temperature decreases, the BCC phase decomposes to the BCC#1 phase that is poor in Nb and Ti (593–765 °C), and then to the BCC#2 phase that is very rich in V but poor in Cr and Nb at T ≤ 593 °C. The $AlTi_3$_DO19 phase forms at 593 °C. The calculated ratio of $(T_{sol} - T_{dec})/T_{sol}$ is 0.46. The Scheil simulation also predicts the formation of a single BCC phase (Figure 8f). Using the true bulk composition reported by Stepanov et al. [11], the equilibration calculation predicts that the C14 Laves phase forms at T = 739–883 °C; and the solidus is 1724 °C. In fact, Stepanov et al. observed the formation of a single BCC phase when homogenized at 1200 °C and the C14 Laves when annealed at 800 °C, which is in agreement with the predictions shown in Figure 8c.

For AlCrNbTiV (Figure 8g), the calculated liquids temperature from the database is 1730 °C; the solid temperature is 1726 °C. The primary BCC phase decomposes to the BCC#1 phase and C14 Laves phase at T ≤ 1206 °C. $AlTi_3$_DO19 forms at T ≤ 563 °C, and the σ phase forms at 712 °C. The calculated ratio of $(T_{sol} - T_{dec})/T_{sol}$ is 0.26. Using the true bulk composition reported in Reference [11], the equilibration calculation predicts that the C14 laves phase starts to form at 1292 °C; the solid temperature is at 1722 °C. In fact, Stepanov et al. [11] observed the formation of the C14 Laves phase in the homogenized state (i.e., at 1200 °C) and for annealed states at 800 °C and 1000 °C. These results generally agree with the predictions shown in Figure 8g.

For CrNbTiZr (Figure 8h), the database predicts that the primary phase is a Nb-rich BCC phase. As the temperature deceases, the Nb content in the BCC phase decreases, while the Ti content increases. At T ≤ 680 °C, the Ti-rich BCC#1 phase and Nb-rich BCC#2 phase form. The C15 Laves phase forms at T ≤ 1384 °C. For CrNbTiVZr (Figure 8i), the primary crystallization phase is a BCC phase that has less Zr and Cr than Nb, V, and Ti, but the Zr and Cr contents continuously increase as the temperature deceases. The C15 Laves phase forms at T ≤ 1297 °C. For both alloys, the predicted stable phases agree well with experiments [13].

In summary, the present CALPHAD calculations using the TCNI8 database successfully predict the formation of a single BCC phase in AlNbTiV, NbTiVZr, and $AlCr_{0.5}$NbTiV, while most empirical rules fail (Table 3). On the other hand, the CALPHAD-predicted crystal structures of intermetallics that form in AlCrNbTiV, CrNbTiZr, and CrNbTiVZr during solidification also agree very well with experiments [11,13]. However, caution should be noted that the database does not

cover thermodynamic descriptions for all constituent ternaries (except the Al-Cr-Ti system) of the Al-Cr-Nb-Ti-V-Zr system. Therefore, the predicted results shown in Figures 8 and 9 are subject to future improvement upon the inclusion of thermodynamic descriptions for all constituent ternaries as well as further optimization with respect to the experimental data wherever available.

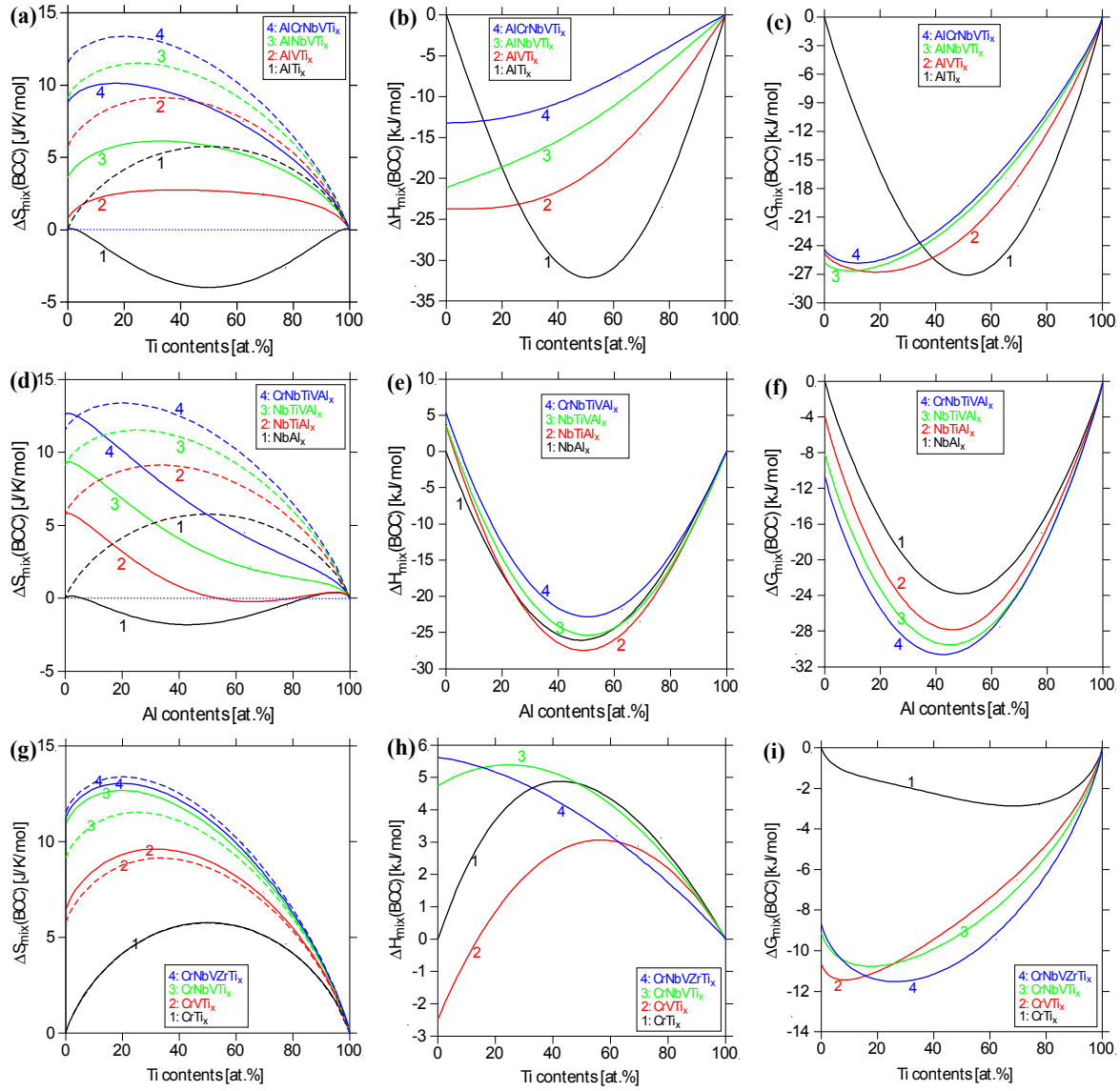

Figure 9. Calculated thermodynamic mixing properties of the BCC phase at 1000 °C: (**a**–**c**) $AlTi_x$, $AlVTi_x$, $AlNbVTi_x$ and $AlCrNbVTi_x$; (**d**–**f**) $NbAl_x$, $NbTiAl_x$, $NbTiVAl_x$ and $CrNbTiVAl_x$; (**g**–**i**) $CrTi_x$, $CrVTi_x$, $CrNbVTi_x$ and $CrNbVZrTi_x$ pseudo-binaries using the TCNI8 database. ΔS_{mix}^{BCC}, ΔH_{mix}^{BCC}, and ΔG_{mix}^{BCC} are the entropy of mixing, enthalpy of mixing, and Gibbs free energy of mixing for the BCC solid-solution phase, respectively. The reference state is the BCC phase at 1000 °C. The dashed curves in (**a**), (**d**), and (**g**) are the ideal configurational entropies.

5. Discussions

5.1. Thermodynamic Mixing Properties of Al-Cr-Nb-Ti-V and Cr-Nb-Ti-V-Zr Systems

In order to lower the density below 7.0 g/cm^3, additions of Al and/or Ti are required for single-phase light-weight HEAs, but excess additions of these elements may cause the formation of brittle intermetallic compounds. Even for the single-phase AlNbTiV, little tensile ductility is expected,

since its compressive fracture strain is very small at room temperature [9]. It is intuitively expected that the formation of strong covalent bonds in a solid solution, which should be reflected in the enthalpy, may cause the embrittlement seen in the alloy. As a consequence, one natural question arises: How do the thermodynamic properties evolve with their additions? Furthermore, as shown in Table 3, those developed-empirical rules basically fail for Al-containing single-phase HEAs, but why?

This subsection attempts to answer these questions by first examining the underlying thermodynamic properties of the BCC phase for selected alloy systems using the CALPHAD method. To eliminate the effect from the pure elements, only the thermodynamic-mixing properties are presented by setting the reference state to the BCC phase at the temperature of interest. The mixing properties of the Al-Cr-Nb-Ti-V system at 1000 °C are shown in Figure 9a–f for varying compositions in binaries and pseudo-binaries with respect to Ti and Al, respectively.

For $AlTi_x$, $AlVTi_x$, $AlNbVTi_x$, and $AlCrNbVTi_x$ alloys (Figure 9a), the total entropies of mixing (ΔS^{BCC}_{mix}) fall well below the respective ideal configurational entropies. Thus, these systems exhibit significant negative excess entropy ($^{ex}S^{BCC}_{mix}$) for the BCC phase. The excess entropy ($^{ex}S^{\phi}_{mix}$) of a solution phase (ϕ) is defined by the difference between the total entropy of mixing (ΔS^{ϕ}_{mix}) and the ideal configurational entropy, as determined in Equation (9):

$$^{ex}S^{\phi}_{mix} = \Delta S^{\phi}_{mix} + R\sum_i c_i \ln c_i \quad (9)$$

Similarly, significant negative excess entropy is also observed for $NbAl_x$, $NbTiAl_x$, $NbTiVAl_x$, and $CrNbTiVAl_x$ alloys (except compositions close to the "terminals" in $CrNbTiVAl_x$ and $NbTiVAl_x$, see Figure 9d). Also, the compositions with the maximum entropy of mixing deviate substantially from their equimolar compositions (see Figure 9d). Note that the ΔS^{BCC}_{mix} values are negative for nearly the entire compositional ranges for both Al-Ti and Al-Nb binaries (Figure 9a,d), suggesting that another entropy source, such as the vibrational entropy of mixing, may be extremely negative and dominate the total entropy of mixing.

The enthalpies of mixing (ΔH^{BCC}_{mix}) (see Figure 9b,e) at the equimolar compositions are very large negative values, and, thus, they contribute significantly to the Gibbs free energies, as shown in Figure 9c,f (Since $\Delta G_{mix} = \Delta H_{mix} - T\Delta S_{mix}$). It is noteworthy that for those M-Ti binary and pseudo-binaries, the lowest ΔH^{BCC}_{mix} (-32 kJ/mol) occurs at 50 at.% Ti in the Al-Ti binary system, but the value for each system becomes less negative quickly with increasing the number of components (Figure 9b). In contrast, for those M-Al binary and pseudo-binaries (see Figure 9e), the lowest ΔH^{BCC}_{mix} for each system occurs in the vicinity of 50 at.% Al, due to the strong ordering tendency to form the CsCl-type B2 phase.

To differentiate the effects of Al and Ti additions, the thermodynamic-mixing properties of the Cr-Nb-Ti-V-Zr system are shown in Figure 9g–i. It is clear that the absence of Al boosts ΔS^{BCC}_{mix} substantially (if one compares Figure 9g to Figure 9a,d). ΔS^{BCC}_{mix} for the Cr-Ti binary behaves almost like the ideal entropy of mixing, while the $CrNbVZrTi_x$ pseudo-binary exhibits the small negative excess entropy of mixing, since its total entropy of mixing is smaller than the ideal configurational entropy. Note that the $CrVTi_x$ and $CrNbVTi_x$ alloys actually exhibit the positive excess entropy, since their total entropies of mixing are greater than their ideal configurational entropies. ΔH^{BCC}_{mix} (Figure 9h) are positive except Ti-poor compositions for the $CrVTi_x$ alloys, implying repulsive interatomic interactions among these refractory metal elements. In this case, the entropy outweighs the enthalpy in the contribution to the Gibbs free energy (Figure 9i).

5.2. Common Issues of Empirical Rules

The empirical rules proposed for the solid-solution HEAs are based on Hume-Rothery rules, thermodynamics, or their combination, and they are established, based on the available experimental data reported in the literature, which includes three main categories of the single-phase solid solution, solid solution + intermetallics, and metallic glasses. As the new experimental data emerge, it is not

surprising to see that those rules may fail for certain compositions. Because most critical values that are proposed in those empirical rules are not scientifically derived. Rather, they are statistically determined based on the available experimental data. For example, the threshold value of the ϕ parameter was originally proposed to be 20, but it is identified to be 7 for light-weight HEAs in the present study. Similarly, the critical δ_r is identified to be $\leq$4.7%, and $\Delta H_{\text{mix}} \geq -16.25\text{kJ} \cdot \text{mol}^{-1}$. A similar phenomenon was also observed for the valence electron concentration (VEC). As reported, FCC phases are found to be stable at higher VEC (>8) and instead BCC phases are stable at lower VEC (<6.87) [17]. However, in light-weight HEAs, although VECs for all the listed light-weight HEAs are smaller than 6, most light-weight HEAs do not present the stable single-phase BCC structure. In other words, these threshold values (e.g., ϕ, δ_r, VEC, etc.) are sensitive to alloy systems and compositions, and, therefore, can be a range rather than a fixed value.

Furthermore, the HEA community has used the empirical enthalpy data for liquids, based on the Miedema model [37] to describe the interatomic interactions in the solid-solution HEAs. This out-of-convenience approach may work in certain cases, but in general, it should be avoided if possible. In fact, a prior study by Gao et al. [27] showed that: "both the sign and absolute value of $\Delta H_{\text{mix}}^{\text{BCC}}$ are not necessarily in accord with $\Delta H_{\text{mix}}^{liq}$: For example, nine alloys exhibit opposite sign while seven alloys show the significant contrast in their absolute values." Furthermore, the accuracy of the liquid enthalpy data from the Miedema model is questionable for certain alloy systems.

In order to address the enthalpy contribution for a multi-component solid solution phase, King et al. [20] first proposed to approximate it as the composition weighted sum of the enthalpy of formation of the constituent binary concentrated solid solution based on the Miedema model. However, this approach does not consider the crystal structure of the solid solution phase, and its robustness requires verification with experimental measurements, CALPHAD modeling, and/or DFT calculations.

In general, the enthalpy of mixing of a solid solution is sensitive to the crystal structure, and the value may vary among FCC, BCC, and HCP structures. As proposed in a recent study [26], the enthalpy of formation (ΔH_f) of solid-solution HEAs with the FCC, BCC, and HCP structures should be used to establish the $\Delta H_f - \delta_r$ relation. For the enthalpy of the formation of single-phase HEAs, readers are referred to recent first-principles density functional calculations [26,35–57], since the experimental enthalpy data for HEAs are not available in the literature.

Φ and Φ_f are designed intentionally to illustrate the thermodynamic competition between the solid-solution phase and intermetallic phases. While the solid-solution phase contains all the principal elements for both models, the intermetallics is represented by the most stable binary compound. Furthermore, both models ignore the entropy of intermetallic compounds, and Φ_f also ignore the mixing of enthalpy for solid solutions, which have been pointed out by Senkov and Miracle [33]. Consequently, both models have thermodynamic flaws, since the phase stability of a multi-component alloy is not determined by the simple comparison of the Gibbs free energy in a solid solution without specifying the crystal structure with that of a hypothetical or binary compound phase; rather, it is determined by the equilibrium condition that the chemical potential of each component should be equal in all phases. In fact, the simple comparison of the Gibbs free energy among phases is only valid for the unary system when to determine phase equilibria.

Also, ignoring the enthalpy contribution of the solid-solution phase, as exercised by Troparevsky et al. [18], can severely underestimate the Gibbs free energy of certain solid-solution phases if the interatomic interactions among constituent elements are very strong, as evidenced in AlCrNbVTi_x (see Figure 9b) and CrNbTiVAl_x (see Figure 9e). The present CALPHAD modeling predicts $\Delta H_{\text{mix}}^{\text{BCC}}$ to be -32, -26, -24, -22, -18, and -12 kJ/mol for AlTi, AlNb, AlNbTi, AlTiV, AlNbTiV, and AlCrNbTiV, respectively, at 1000 °C. On the other hand, the enthalpies of formation for solid-solution phases and intermetallics estimated from the Miedema model may suffer from the inaccuracy issue. Furthermore, using the most stable binary compound to represent the competing intermetallic phase in a multi-component system may overestimate its thermodynamic stability. The combined consequence

is that these models will underestimate the likely compositions that may form single-phase solid solutions. For example, forming a single BCC-phase in AlNbTiV was predicted by CALPHAD modeling (Figure 8a,d), and was experimentally verified [9], but Φ and Φ_f parameters as well as the $\Delta H_f - \delta_r$ relation fail to predict the formation of a single solid-solution phase. Nonetheless, the calculated Φ and Φ_f values generally show remarkable similarity for alloys listed in Table 2 except certain compositions that contain Al and Mg and/or Li, and those that contain Hf. The similarity between Φ and Φ_f shown in Table 2 can be understood, through the ratio

$$\frac{\Phi}{\Phi_f} = \left|\frac{\Delta H_{\text{mix}}^{ss} - T_{\text{m}}\Delta S_{\text{mix}}}{T_{\text{ann}}\Delta S_{\text{mix}}}\right| \left|\frac{\Delta H_f^{\text{DFT}}}{\Delta H_f^{Mid}}\right| \approx \left|\frac{\Delta H_{\text{mix}}^{ss}}{T_{\text{ann}}\Delta S_{\text{mix}}} - 1.82\right| \left|\frac{\Delta H_f^{\text{DFT}}}{\Delta H_f^{Mid}}\right| \quad (10)$$

where Φ and Φ_f can be obtained from Equations (7) and (8). For those alloys with similar values of Φ and Φ_f, $\frac{\Delta H_{\text{mix}}^{ss}}{T_{\text{ann}}\Delta S_{\text{mix}}} \approx -1$ and $\left|\frac{\Delta H_f^{\text{DFT}}}{\Delta H_f^{Mid}}\right| \approx \frac{1}{3}$ can be found from the calculated corresponding parameters, which lead to the ratio of $\frac{\Phi}{\Phi_f} \approx 1$. The special ratio between ΔH_f^{Mid} and ΔH_f^{DFT} among those alloys may be attributed to the intrinsic connection between the Mediema model and DFT calculations.

Lastly, for the Al-containing HEAs, the actual entropy of mixing can be substantially depressed due to strong interatomic interactions between Al and TMs. For example, the calculated ΔS_{mix} are -4, -2, +2, +3, +6, and +10 J/(mol·K) for AlTi, AlNb, AlNbTi, AlTiV, AlNbTiV, and AlCrNbTiV, respectively; they are well below the corresponding ideal configurational entropy (Figure 9a,d), especially for the binary and ternary alloys. The much lowered entropy for the Al-containing HEAs may contribute to the additional uncertainty when predicting the solid-solution formation, using those empirical rules.

5.3. Perspectives of Future Design of Light-Weight HEAs

As demonstrated in the present and other studies, the CALPHAD method is the ideal approach to predict the phase stability in multi-component systems, such as HEAs. The main limitation of CALPHAD is the reliability of the thermodynamic database. A robust self-consistent database for HEAs requires the optimization of all constituent binaries and ternaries over the entire composition and temperature ranges. When such a database is not available, reliance on empirical rules, phase-diagram inspections, and density functional theory (DFT) modeling may be necessary. In fact, Gao et al. [26] has demonstrated an effective approach that combines the phase-diagram inspection, CALPHAD modeling, first-principles DFT calculations, and *ab initio* molecular dynamics simulations, and suggested hundreds of new single-phase equimolar HEA compositions. For example, Gao suggested quaternary and higher-order equimolar compositions in the Dy-Er-Gd-Ho-Lu-Sc-Sm-Tb-Tm-Y system, Ba-Ca-Eu-Sr-Yb system, Mo-Nb-Ta-Ti-V-W system, and Mo-Nb-Re-Ta-Ti-V-W system [26].

Strong attractive interactions between Al and TMs, and between Ti and late TMs (such as Mn, Fe, Co, and Ni) cause the formation of very stable intermetallic compounds, and, thus, the formation of single-phase HEAs that contain Al and/or Ti in high contents is difficult. Therefore, the total number of single-phase light-weight HEAs is very limited, and their densities are generally above 5.5 g/cm^3 (see Table 2). On the other hand, for practical applications, the alloy compositions do not need to be equimolar or near-equimolar ratios, and most importantly, multi-phase microstructures are usually desirable to balance various materials properties, especially the excellent combination of strength and ductility. Therefore, from the application point of view, a rational approach for the future design of light-weight HEAs with a density less than 5.0 g/cm^3 can be described below:

(1) Identify the main alloying elements in addition to the dominant principal element (such as Ti, Al, or Mg), based on the target-properties requirement.
(2) Use the high-entropy concept to adjust the bulk composition so as to maximize the solubility of key strengthening (or ductilizing, anti-oxidation, etc.) alloying elements.

(3) Predict phase stability using the CALPHAD method, DFT modeling, and/or empirical criteria, and design processing and heat-treatment routes to optimize the microstructure.
(4) Fabricate the down-selected alloys and characterize their microstructures and mechanical (and other) properties.
(5) Refine alloy design by repeating the above procedures.

6. Conclusions

The present study investigated the phase formation in $Al_xCrFeMnTi_y$, assessed various empirical rules pertaining to light-weight HEAs, and carried out CALPHAD modeling on Al-Cr-Nb-Ti-V and Cr-Nb-Ti-V-Zr systems. The following conclusions were reached:

(1) Empirical rules are not conclusive in predicting solid-solution formation, and they are susceptible to the alloy systems and compositions that are assessed. As new experimental data emerge, these rules are subject to reevaluation. Consequently, the proposed threshold values pertaining to those empirical rules are sensitive to alloy systems and compositions, and can fluctuate within a range of values. For light-weight HEAs, the following criteria have been identified: $\phi_c \geq 7$, $\delta_r \leq 4.7\%$, and $\Delta H_{\text{mix}} \geq -16.25\text{kJ} \cdot \text{mol}^{-1}$.
(2) The combination of Φ or Φ_f with δ_r appears to be more effective criteria than with ΔH_{mix} or Ω to differentiate SS from SS + IM.
(3) For certain HEAs with strong interatomic interactions among constituent elements, such as Al-containing HEAs, empirical rules may severely underestimate the free energies of the solid-solution phases by ignoring the enthalpy contribution of the solid-solution phase.
(4) The present CALPHAD modeling using the TCNI8 database successfully predicts the single BCC phase in AlNbTiV, $Al_{0.5}$NbTiV, and NbTiVZr, while most empirical rules fail to do so.
(5) The calculated entropies of mixing ($\Delta S_{\text{mix}}^{\text{BCC}}$) for the BCC phase at 1000 °C are −4, −2, +2, +3, +6, and +10 J/(mol·K) for AlTi, AlNb, AlNbTi, AlTiV, AlNbTiV, and AlCrNbTiV, respectively; they are well below the corresponding ideal configurational entropy, especially for the binary and ternary alloys. Therefore, these systems exhibit noticeable negative excess entropy with the BCC structure.
(6) The present CALPHAD modeling predicts that the enthalpies of mixing ($\Delta H_{\text{mix}}^{\text{BCC}}$) for the BCC phase at 1000 °C are −32, −26, −24, −22, −18, and −12 kJ/mol for AlTi, AlNb, AlNbTi, AlTiV, AlNbTiV, and AlCrNbTiV, respectively.
(7) Forming Al-containing equimolar light-weight HEAs with a density less than 5.5 g/cm^3 is very challenging due to very attractive interatomic interactions between Al and TMs. As such, future efforts could be shifted towards Al-rich (or Ti-rich, or Mg-rich) alloys that contain large amounts of desirable solute elements, which may dissolve in solution and/or promote the formation of beneficial precipitates, taking advantage of the high-entropy concept.

Acknowledgments: The authors very much appreciate the support from the U.S. Army Office Project (W911NF-13-1-0438) with the program manager, David M. Stepp. Peter K. Liaw would like to acknowledge the Department of Energy (DOE), Office of Fossil Energy, National Energy Technology Laboratory (DE-FE-0008855, DE-FE-0024054, and DE-FE-0011194), with Vito N. Cedro, Richard J. Dunst, and Jessica Mullen as program managers. Peter K. Liaw also thanks the support from the National Science Foundation (CMMI-1100080 and DMR-1611180) with the program director, Clark Cooper and Diana Farkas. The present work was also funded by the Cross-Cutting Technologies Program at the National Energy Technology Laboratory (NETL)—Strategic Center for Coal, managed by Robert Romanosky (Technology Manager) and Charles Miller (Technology Monitor). The Research was executed through NETL's Office of Research and Development's Innovative Process Technologies (IPT) Field Work Proposal. Research performed by the AECOM staff was conducted under the RES contract DE-FE-0004000. Yong Zhang would like to thank the support from National Natural Science Foundation of China (NSFC) (51471025). All authors have read and approved the final manuscript.

Author Contributions: Rui Feng and Chanho Lee conducted the experiments; Michael C. Gao and Jeffrey A. Hawk performed the CALPHAD modeling; Rui Feng, Michael C. Gao, Chanho Lee, Michael Mathes, Tingting Zuo, and Shuying Chen analyzed the data and prepared the figures; Rui Feng and Michael C. Gao wrote the main manuscript; Michael C. Gao, Yong Zhang, and Peter K. Liaw jointly supervised the work. All the authors contributed to the discussion and revision of the content.

Conflicts of Interest: The authors declare no conflict of interest. This project was partially funded by the Department of Energy, National Energy Technology Laboratory, an agency of the United States Government, through a support contract with AECOM. Neither the United States Government nor any agency thereof, nor any of their employees, nor AECOM, nor any of their employees, makes any warranty, expressed or implied, or assumes any legal liability or responsibility for the accuracy, completeness, or usefulness of any information, apparatus, product, or process disclosed, or represents that its use would not infringe privately owned rights. Reference herein to any specific commercial product, process, or service by trade name, trademark, manufacturer, or otherwise, does not necessarily constitute or imply its endorsement, recommendation, or favoring by the United States Government or any agency thereof. The views and opinions of authors expressed herein do not necessarily state or reflect those of the United States Government or any agency thereof.

References

1. Cantor, B.; Chang, I.; Knight, P.; Vincent, A. Microstructural development in equiatomic multicomponent alloys. *Mater. Sci. Eng. A* **2004**, 375–377. [CrossRef]
2. Yeh, J.W.; Chen, S.K.; Lin, S.J.; Gan, J.Y.; Chin, T.S.; Shun, T.T.; Tsau, C.H.; Chang, S.Y. Nanostructured high-entropy alloys with multiple principal elements: Novel alloy design concepts and outcomes. *Adv. Eng. Mater.* **2004**, *6*, 299–303. [CrossRef]
3. Zhang, Y.; Zuo, T.T.; Tang, Z.; Gao, M.C.; Dahmen, K.A.; Liaw, P.K.; Lu, Z.P. Microstructures and properties of high-entropy alloys. *Prog. Mater. Sci.* **2014**, *61*. [CrossRef]
4. Zhang, Y.; Zhou, Y.J.; Lin, J.P.; Chen, G.L.; Liaw, P.K. Solid-solution phase formation rules for multi-component alloys. *Adv. Eng. Mater.* **2008**, *10*, 534–538. [CrossRef]
5. Santodonato, L.J.; Zhang, Y.; Feygenson, M.; Parish, C.M.; Gao, M.C.; Weber, R.J.; Neuefeind, J.C.; Tang, Z.; Liaw, P.K. Deviation from high-entropy configurations in the atomic distributions of a multi-principal-element alloy. *Nat. Commun.* **2015**, *6*, 5964. [CrossRef] [PubMed]
6. Gao, M.C.; Yeh, J.W.; Liaw, P.K.; Zhang, Y. *High-Entropy Alloys: Fundamentals and Applications*; Springer: Cham, Switzerland, 2016.
7. Youssef, K.M.; Zaddach, A.J.; Niu, C.; Irving, D.L.; Koch, C.C. A novel low-density, high-hardness, high-entropy alloy with close-packed single-phase nanocrystalline structures. *Mater. Res. Lett.* **2015**, *3*, 95–99. [CrossRef]
8. Liu, S.; Gao, M.C.; Liaw, P.K.; Zhang, Y. Microstructures and mechanical properties of $Al_xCrFeNiTi_{0.25}$ alloys. *J. Alloy. Compd.* **2015**, *619*, 610–615. [CrossRef]
9. Stepanov, N.; Shaysultanov, D.; Salishchev, G.; Tikhonovsky, M. Structure and mechanical properties of a light-weight AlNbTiV high entropy alloy. *Mater. Lett.* **2015**, *142*, 153–155. [CrossRef]
10. Stepanov, N.; Yurchenko, N.Y.; Shaysultanov, D.; Salishchev, G.; Tikhonovsky, M. Effect of Al on structure and mechanical properties of $Al_xNbTiVZr$ (x = 0, 0.5, 1, 1.5) high entropy alloys. *Mater. Sci. Technol.* **2015**, *31*, 1184–1193. [CrossRef]
11. Stepanov, N.; Yurchenko, N.Y.; Skibin, D.; Tikhonovsky, M.; Salishchev, G. Structure and mechanical properties of the $AlCr_xNbTiV$ (x = 0, 0.5, 1, 1.5) high entropy alloys. *J. Alloy. Compd.* **2015**, *652*, 266–280. [CrossRef]
12. Senkov, O.N.; Senkova, S.V.; Miracle, D.B.; Woodward, C.F. Mechanical properties of low-density, refractory multi-principal element alloys of the Cr–Nb–Ti–V–Zr system. *Mater. Sci. Eng. A* **2013**, *565*, 51–62. [CrossRef]
13. Senkov, O.N.; Senkova, S.V.; Woodward, C.F.; Miracle, D.B. Low-density, refractory multi-principal element alloys of the Cr–Nb–Ti–V–Zr system: Microstructure and phase analysis. *Acta Mater.* **2013**, *61*, 1545–1557. [CrossRef]
14. Chen, H.; Kauffmann, A.; Gorr, B.; Schliephake, D.; Seemüller, C.; Wagner, J.; Christ, H.J.; Heilmaier, M. Microstructure and mechanical properties at elevated temperatures of a new Al-containing refractory high-entropy alloy Nb-Mo-Cr-Ti-Al. *J. Alloy. Compd.* **2016**, *661*, 206–215. [CrossRef]
15. Senkov, O.N.; Woodward, C.F.; Miracle, D.B. Microstructure and properties of aluminum-containing refractory high-entropy alloys. *JOM* **2014**, *66*, 2030–2042. [CrossRef]

16. Yang, X.; Zhang, Y. Prediction of high-entropy stabilized solid-solution in multi-component alloys. *Mater. Chem. Phys.* **2012**, *132*, 233–238. [CrossRef]
17. Guo, S.; Ng, C.; Lu, J.; Liu, C.T. Effect of valence electron concentration on stability of fcc or bcc phase in high entropy alloys. *J. Appl. Phys.* **2011**, *109*, 103505. [CrossRef]
18. Troparevsky, M.C.; Morris, J.R.; Kent, P.R.; Lupini, A.R.; Stocks, G.M. Criteria for predicting the formation of single-phase high-entropy alloys. *Phys. Rev. X* **2015**, *5*, 011041. [CrossRef]
19. Ye, Y.F.; Wang, Q.; Lu, J.; Liu, C.T.; Yang, Y. Design of high entropy alloys: A single-parameter thermodynamic rule. *Scr. Mater.* **2015**, *104*, 53–55. [CrossRef]
20. King, D.J.M.; Middleburgh, S.C.; McGregor, A.G.; Cortie, M.B. Predicting the formation and stability of single phase high-entropy alloys. *Acta Mater.* **2016**, *104*, 172–179. [CrossRef]
21. Poletti, M.G.; Battezzati, L. Electronic and thermodynamic criteria for the occurrence of high entropy alloys in metallic systems. *Acta Mater.* **2014**, *75*, 297–306. [CrossRef]
22. Gao, M.C.; Alman, D.E. Searching for next single-phase high-entropy alloy compositions. *Entropy* **2013**, *15*, 4504–4519. [CrossRef]
23. Ye, Y.F.; Wang, Q.; Lu, J.; Liu, C.T.; Yang, Y. The generalized thermodynamic rule for phase selection in multicomponent alloys. *Intermetallics* **2015**, *59*, 75–80. [CrossRef]
24. Wang, Z.J.; Qiu, W.F.; Yang, Y.; Liu, C.T. Atomic-size and lattice-distortion effects in newly developed high-entropy alloys with multiple principal elements. *Intermetallics* **2015**, *64*, 63–69. [CrossRef]
25. Wang, Z.J.; Huang, Y.H.; Yang, Y.; Wang, J.; Liu, C.T. Atomic-size effect and solid solubility of multicomponent alloys. *Scr. Mater.* **2015**, *94*, 28–31. [CrossRef]
26. Gao, M.C. Design of high-entropy alloys. In *High-Entropy Alloys: Fundamentals and Applications*; Gao, M.C., Yeh, J.W., Liaw, P.K., Zhang, Y., Eds.; Springer: Cham, Switzerland, 2016; pp. 369–398.
27. Gao, M.C.; Carney, C.S.; Doğan, Ö.N.; Jablonksi, P.D.; Hawk, J.A.; Alman, D.E. Design of refractory high-entropy alloys. *JOM* **2015**, *67*, 2653–2669. [CrossRef]
28. Gao, M.C.; Zhang, B.; Guo, S.M.; Qiao, J.W.; Hawk, J.A. High-entropy alloys in hexagonal close packed structure. *Metall. Mater. Trans. A* **2016**, *47*, 3322–3332. [CrossRef]
29. Zhang, Y.; Lu, Z.P.; Ma, S.G.; Liaw, P.K.; Tang, Z.; Cheng, Y.Q.; Gao, M.C. Guidelines in predicting phase formation of high-entropy alloys. *MRS Commun.* **2014**, *4*, 57–62. [CrossRef]
30. Hammond, V.H.; Atwater, M.A.; Darling, K.A.; Nguyen, H.Q.; Kecskes, L.J. Equal-channel angular extrusion of a low-density high-entropy alloy produced by high-energy cryogenic mechanical alloying. *JOM* **2014**, *66*, 2021–2029. [CrossRef]
31. Yang, X.; Chen, S.Y.; Cotton, J.D.; Zhang, Y. Phase stability of low-density, multiprincipal component alloys containing aluminum, magnesium, and lithium. *JOM* **2014**, *66*, 2009–2020. [CrossRef]
32. Li, R.; Gao, J.C.; Fan, K. Microstructure and mechanical properties of MgMnAlZnCu high entropy alloy cooling in three conditions. *Mater. Sci. Forum* **2011**, *686*, 235–241. [CrossRef]
33. Senkov, O.N.; Miracle, D.B. A new thermodynamic parameter to predict formation of solid solution or intermetallic phases in high entropy alloys. *J. Alloy. Compd.* **2016**, *658*, 603–607. [CrossRef]
34. Widom, M.; Huhn, W.P.; Maiti, S.; Steurer, W. Hybrid Monte Carlo/molecular dynamics simulation of a refractory metal high entropy alloy. *Metall. Mater. Trans. A* **2014**, *45*, 196–200. [CrossRef]
35. Widom, M. Prediction of structure and phase transformations. In *High-Entropy Alloys: Fundamentals and Applications*; Gao, M.C., Yeh, J.W., Liaw, P.K., Zhang, Y., Eds.; Springer: Cham, Switzerland, 2016; pp. 267–298.
36. Gao, M.C.; Niu, C.; Jiang, C.; Irving, D.L. Applications of special quasi-random structures to high-entropy alloys. In *High-Entropy Alloys: Fundamentals and Applications*; Gao, M.C., Yeh, J.W., Liaw, P.K., Zhang, Y., Eds.; Springer: Cham, Switzerland, 2016; pp. 333–368.
37. De Boer, F.R. *Cohesiodn in Metals: Transition Metal Alloys*; North-Holland: Amsterdam, NY, USA, 1988; p. 785.
38. King, D.J.M.; McGregor, A.G. Alloy Search and Predict. Available online: www.alloyASAP.com (accessed on 6 September 2016).
39. Senkov, O.N.; Wilks, G.B.; Miracle, D.B.; Chuang, C.; Liaw, P.K. Refractory high-entropy alloys. *Intermetallics* **2010**, *18*, 1758–1765. [CrossRef]
40. Takeuchi, A.; Amiya, K.; Wada, T.; Yubuta, K.; Zhang, W. High-entropy alloys with a hexagonal close-packed structure designed by equi-atomic alloy strategy and binary phase diagrams. *JOM* **2014**, *66*, 1984–1992. [CrossRef]

41. Zhao, Y.J.; Qiao, J.W.; Ma, S.G.; Gao, M.C.; Yang, H.J.; Chen, M.W.; Zhang, Y. A hexagonal close-packed high-rntropy alloy: The effect of entropy. *Mater. Des.* **2016**, *96*, 10–15.
42. Feuerbacher, M.; Heidelmann, M.; Thomas, C. Hexagonal high-entropy alloys. *Mater. Res. Lett.* **2015**, *3*, 1–6. [CrossRef]
43. Kao, Y.F.; Chen, T.J.; Chen, S.K.; Yeh, J.W. Microstructure and mechanical property of as-cast, -homogenized, and -deformed $Al_xCoCrFeNi$ ($0 \leq x \leq 2$) high-entropy alloys. *J. Alloy. Compd.* **2009**, *488*, 57–64. [CrossRef]
44. Wu, Y.D.; Cai, Y.H.; Wang, T.; Si, J.J.; Zhu, J.; Wang, Y.D.; Hui, X.D. A refractory $Hf_{25}Nb_{25}Ti_{25}Zr_{25}$ high-entropy alloy with excellent structural stability and tensile properties. *Mater. Lett.* **2014**, *130*, 277–280. [CrossRef]
45. Senkov, O.; Scott, J.; Senkova, S.; Meisenkothen, F.; Miracle, D.; Woodward, C. Microstructure and elevated temperature properties of a refractory TaNbHfZrTi alloy. *J. Mater. Sci.* **2012**, *47*, 4062–4074. [CrossRef]
46. Sundman, B.; Jansson, B.; Andersson, J.O. The thermo-calc databank system. *Calphad* **1985**, *9*, 153–190. [CrossRef]
47. Zhang, B.; Gao, M.C.; Zhang, Y.; Yang, S.; Guo, S.M. Senary refractory high-entropy alloy MoNbTaTiVW. *Mater. Sci. Technol.* **2015**, *31*, 1207–1213. [CrossRef]
48. Zhang, B.; Gao, M.C.; Zhang, Y.; Guo, S.M. Senary refractory high-entropy alloy $Cr_xMoNbTaVW$. *Calphad* **2015**, *51*, 193–201. [CrossRef]
49. Gao, M.C.; Zhang, B.; Yang, S.; Guo, S.M. Senary refractory high-entropy alloy HfNbTaTiVZr. *Metall. Mater. Trans. A* **2016**, *47*, 3333–3345. [CrossRef]
50. Zhang, C.; Gao, M.C. CALPHAD modeling of high-entropy alloys. In *High-Entropy Alloys: Fundamentals and Applications*; Gao, M.C., Yeh, J.W., Liaw, P.K., Zhang, Y., Eds.; Springer: Cham, Switzerland, 2016; pp. 399–444.
51. Yao, H.W.; Qiao, J.W.; Gao, M.C.; Hawk, J.A.; Ma, S.G.; Zhou, H.F.; Zhang, Y. NbTaV-(Ti, W) refractory high entropy alloys. *Mater. Sci. Eng. A* **2016**, submitted for publication. [CrossRef]
52. Zhang, C.; Zhang, F.; Chen, S.L.; Cao, W.S. Computational thermodynamics aided high-entropy alloy design. *JOM* **2012**, *64*, 839–845. [CrossRef]
53. Zhang, F.; Zhang, C.; Chen, S.L.; Zhu, J.; Cao, W.S.; Kattner, U. An understanding of high entropy alloys from phase diagram calculations. *Calphad* **2014**, *45*. [CrossRef]
54. Zhang, C.; Zhang, F.; Diao, H.; Gao, M.C.; Tang, Z.; Liaw, P.K. Understanding phase stability of Al-Co-Cr-Fe-Ni high entropy alloys. *Mater. Des.* **2016**, *109*, 425–433. [CrossRef]
55. Gulliver, G.H. The quantitative effect of rapid cooling upon the constitution of binary alloys. *J. Inst. Met.* **1913**, *9*, 120–157.
56. Scheil, E. Comments on the layer crystal formation. *Z. Metallkd.* **1942**, *34*, 70–72.
57. Tian, F.; Wang, Y.; Irving, D.L.; Vitos, L. Applications of coherent potential approximation to HEAs. In *High-Entropy Alloys: Fundamentals and Applications*; Gao, M.C., Yeh, J.W., Liaw, P.K., Zhang, Y., Eds.; Springer: Cham, Switzerland, 2016; pp. 299–332.